Computer Methods in Applied Mechanics and Engineering 437 (2025) 117783

Contents lists available at ScienceDirect

Comput. Methods Appl. Mech. Engrg.

journal homepage: www.elsevier.com/locate/cma

Multiphysics simulation of crystal growth with moving boundaries in FEniCS

Arved Wintzer [a], Bilen Emek Abali [b,*], Kaspars Dadzis [a,*]

[a] Leibniz-Institut für Kristallzüchtung (IKZ), Materials Science Department, Max-Born-Str. 2, 12489 Berlin, Germany
[b] Uppsala University, Department of Materials Science and Engineering, Box 35, 751 03 Uppsala, Sweden

ARTICLE INFO

Keywords:
Multiphysics
Crystal growth
FEniCS
Finite element method
Simulation
Czochralski method

ABSTRACT

Crystal growth processes and the Czochralski process in particular involves various physical phenomena such as heat transfer, phase change or liquid flows and requires a coupled multiphysical model for realistic numerical simulations. In this work, a new and extendable model is developed using the open-source software FEniCS. Basic equations for electromagnetic induction, heat conduction and radiation as well as phase change are thoroughly derived up to a finite element form and discussed together with the assumed boundary conditions and approximations. Verification of the FEniCS model with an analytical case demonstrated an accuracy with an error below 1%. A comparison with experimental results and numerical data from a similar model achieved a good agreement and showed opportunities for further improvement of melt flow modeling in particular.

1. Introduction

Multiphysics computations are able to simulate sophisticated phenomena owing to advanced capabilities of new algorithms implemented in modern programming languages. Various open-source software tools for multiphysics simulations exist, e.g. finite element method (FEM) based libraries for implementation of own solvers like deal.ii [1], Goma [2], FEniCS [3], GetDP [4], Moose [5], ready-to-use FEM solvers like Elmer [6], or finite volume method based tools like OpenFOAM [7], SU2 [8], that are successfully applied in both industry and science. Based on such packages, different models are used in electromagnetism [9,10] and their reduced order digital twins [11,12]. Simulation of multiphysics problems with open-source tools opens new possibilities for testing and implementing novel ideas as well as building upon existing solution procedures. In this work, we develop a digital twin of crystal growth and implement a multiphysics computation by using open-source packages. The code is publicly available to motivate its further use.

The Czochralski (CZ) growth process is one of the main methods for production of bulk single crystals, e.g., classical semiconductors like Si, Ge, GaAs, or oxides like Ga_2O_3, which are used in computer chips, solar cells, or power electronics [13,14]. The CZ process involves different physical phenomena such as heat transfer including radiation and phase change, electromagnetism, and melt and gas flows. Various numerical models of CZ growth exist; among others, we refer to [15–17] for 2D and [18–20] for 2D-3D modeling of Si, [21,22] for 2D modeling of Ge, [23,24] for 2D modeling GaAs, and [25–29] for 2D and 2D-3D modeling of different oxide crystals. Most of the models in the literature are implemented in commercial software, e.g. CGSim or Ansys, or in-house codes, without publishing the underlying source code and making it difficult to fully examine the applied algorithms [30]. However, this is crucial for reproduction and critical assessment, e.g., of assumptions made in the development of new flow

* Corresponding authors.
E-mail addresses: bilenemek@abali.org (B.E. Abali), kaspars.dadzis@ikz-berlin.de (K. Dadzis).

https://doi.org/10.1016/j.cma.2025.117783
Received 22 October 2024; Received in revised form 19 December 2024; Accepted 20 January 2025
Available online 30 January 2025

Table 1
Material properties taken from [30,36–41].

Material	Mass density	El. conductivity	Emissivity	Heat capacity	Heat conductivity
Air	$1.189\,\mathrm{kg\,m^{-3}}$	0	–	$1006\,\mathrm{J\,kg^{-1}\,K^{-1}}$	$26\,\mathrm{mW\,m^{-1}\,K^{-1}}$
Copper	–	–	0.2	–	$390\,\mathrm{W\,m^{-1}\,K^{-1}}$
Graphite	$1730\,\mathrm{kg\,m^{-3}}$	$5.88 \times 10^4\ \mathrm{S\,m^{-1}}$	0.7	–	$65\,\mathrm{W\,m^{-1}\,K^{-1}}$
Insulation	$220\,\mathrm{kg\,m^{-3}}$	$195\,\mathrm{S\,m^{-1}}$	0.7	–	$0.2\,\mathrm{W\,m^{-1}\,K^{-1}}$
Steel 1.4541	$7900\,\mathrm{kg\,m^{-3}}$	$1.37 \times 10^6\ \mathrm{S\,m^{-1}}$	0.2	–	$15\,\mathrm{W\,m^{-1}\,K^{-1}}$
Tin (liquid)	$6980\,\mathrm{kg\,m^{-3}}$	$2.08 \times 10^6\ \mathrm{S\,m^{-1}}$	0.1	$253\,\mathrm{J\,kg^{-1}\,K^{-1}}$	$29\,\mathrm{W\,m^{-1}\,K^{-1}}$
Tin (solid)	$7170\,\mathrm{kg\,m^{-3}}$	$4.38 \times 10^6\ \mathrm{S\,m^{-1}}$	0.1	$244\,\mathrm{J\,kg^{-1}\,K^{-1}}$	$60\,\mathrm{W\,m^{-1}\,K^{-1}}$

Table 2
Characteristic values of the crystal growth process for melt, crystal and gas domain. The flow velocities are estimated values.

Characteristic value	Symbol	Crystal	Melt	Gas
Length (diameter)	L_0	0.008 m	0.1 m	0.4 m
Velocity	v_0	$1\,\mathrm{mm\,min^{-1}}$	$0.01\,\mathrm{m\,s^{-1}}$	$1\,\mathrm{m\,s^{-1}}$
Time	$t_0 = \frac{L_0}{v_0}$	8 min	10 s	0.4 s

modeling approaches such as [31] as well as new techniques for variable crystal diameter such as [16]. The authors have already published a comprehensive review [30] on all physical capabilities and validation status of these models. We emphasize that there is a need for transparent and explainable implementations.

In this work, a new model for the CZ process is proposed. First, we discuss the problem statement in Section 2 and governing equations with material parameters in Section 3. The coupled and nonlinear field equations are implemented by means of the open-source software FEniCSx [3,32,33]. Due to the rotational symmetry of the investigated system, a 2D axisymmetric formulation is used. The model includes the time-harmonic electromagnetism of induction heating and steady-state heat transfer. We propose a novel interface tracking approach between solid and fluid for an accurate prediction. Modeling this interface is difficult since between the melt and crystal phases, a solidification takes place by releasing latent heat. This energy contribution is released at the computed melting point isotherm and the mesh is iteratively deformed so that the melt/crystal boundary matches this isotherm. The resulting mesh distortion is smoothed by using Poisson's equation. This proposed approach as well as other numerical techniques are described in Section 4. For verification in Section 5, the simulation of the induction heating is employed since this problem has an analytical solution. For validation in Section 6, the complete model of CZ process has been compared to the data obtained in an experimental benchmark case. Such experiments are being developed in the NEMOCRYS project [34] focusing on easy experimental access for various in-situ measurements.

2. Problem statement

The CZ growth process consists of several steps:

- First, raw material is molten in a crucible by heating from the bottom and sides.
- Second, a small single crystalline seed is dipped into the melt. It partially melts, and a solid/liquid interface with a small meniscus is formed.
- Third, after temperature homogenization, the seed is pulled slowly upward, and the liquid raw material solidifies at the interface between seed and melt, forming a crystal. The motion of the seed opposes the growth process as the melt is solidifying and the solid/liquid interface is moving downward with respect to the crystal.
- Eventually, the obtained crystal is detached from the melt and left to cool down.

In this study, the third process step is modeled, which accounts for most of the process time, and has a major impact on crystal quality. The experiment from [35] is applied as a reference process because it offers extensive validation possibilities through in-situ measurements at lower temperatures using tin (Sn, melting point 232 °C) compared to standard processes operated at high temperatures (e.g. 1412 °C for Si). This experiment has been successfully applied to validate a crystal growth model in [30].

A sketch and photograph of the growth furnace are shown in Fig. 1. The system consists of a steel furnace vessel equipped with two axes: on the bottom axis, a crucible (inner diameter of 100 mm) containing the liquid raw material is mounted; the top axis carries the seed and the crystal. The crucible is heated inductively using a water-cooled copper coil. The coil is supplied with a frequency of 13.4 kHz, and the current is controlled to maintain a constant temperature at a fixed position in the melt. During the process, temperatures at various positions, e.g. in the crystal, are measured with thermocouples (type K); crucible temperature is measured at two circumferential positions by a thermocouple (type K) and resistance temperature sensor (Pt100); melt temperature is measured by a thermocouple and resistance temperature sensor (Pt100). Current in the inductor is measured by a Rogowski coil. An extensive description of the growth furnace and the measurement setup can be found in [35].

The material properties and the characteristic quantities, e.g. lengths and velocities, describing the process are listed in Tables 1 and 2, respectively. They are applied to estimate the influence of various physical processes by means of dimensionless numbers in the following section.

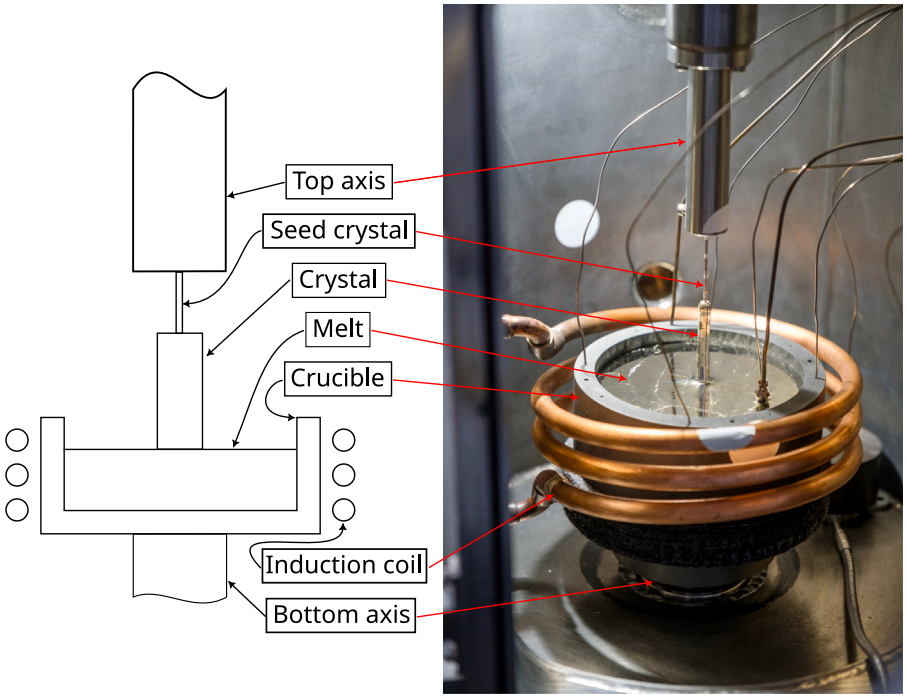

Fig. 1. Schematic sketch and photograph of the experimental setup.

3. Physical equations

The focus of this work is to model the 2D axisymmetric heat distribution during the growth process together with the shape of the crystallization front as well as the electromagnetic heating. Solving the underlying physical equations directly (i.e. Maxwell's equations, energy, momentum, and mass balance) is possible but computationally costly, as the problem allows for several simplifications. In this section, therefore, a reduced order model is introduced and derived by discussing all the underlying assumptions.

3.1. Electromagnetism

Electromagnetism is described by the balance of magnetic flux (also called Faraday's law) and the balance of electric charge [42, Chap. 3], as follows:

$$\begin{aligned}\left(\int_{\mathcal{S}} \boldsymbol{B}\cdot\boldsymbol{n}\,\mathrm{d}a\right)^{\cdot} &= -\int_{\partial\mathcal{S}} \boldsymbol{\mathcal{E}}\cdot\boldsymbol{v}\,\mathrm{d}\ell\ ,\\ \left(\int_{\Omega} q\,\mathrm{d}v\right)^{\cdot} &= -\int_{\partial\Omega} \boldsymbol{J}\cdot\boldsymbol{n}\,\mathrm{d}a\end{aligned} \tag{1}$$

with electric field, $\boldsymbol{\mathcal{E}}$ in $\mathrm{V\,m^{-1}}$, magnetic flux density $\boldsymbol{B}$ in T, (electric) charge density, $q = \rho z$ in $\mathrm{C\,m^{-3}}$, mass density, ρ in $\mathrm{kg\,m^{-3}}$, specific (electric) charge, z in $\mathrm{C\,kg^{-1}}$, and electric current, $\boldsymbol{J}$ in $\mathrm{A\,m^{-2}} \triangleq \mathrm{C\,s^{-1}\,m^{2}}$. The former is a balance of magnetic flux evaluated on a moving surface, $\mathcal{S}$, with its boundaries, $\partial\mathcal{S}$. The latter is a balance of charge within a fixed volume, Ω, with its boundaries (closure), $\partial\Omega$. Both domains are open systems (also called a control domain); after a well-known argumentation, each of these equations deliver 2 Maxwell equations with magnetic field intensity (current potential), $\boldsymbol{H}$ in $\mathrm{A\,m^{-1}}$, and dielectric displacement field (charge potential), $\boldsymbol{D}$ in $\mathrm{C\,m^{-2}}$. Electric charge and current are for free and bound charges, hence, charge and current potentials are also for free and bound charges. For an in-depth discussion of electromagnetism and thermomechanics coupling, we refer to [43–45].

In this work, the magnetohydrodynamic (MHD) approximation of the Maxwell's equations is used by following these assumptions:

- non-relativistic velocities, $v^2 \ll c_0^2$, with velocity of mass v, speed of light $c_0 \approx 2.998 \times 10^8\,\mathrm{m\,s^{-1}}$,
- negligible magnetic polarization, $\boldsymbol{H} = \frac{\boldsymbol{B}}{\mu}$, with materials magnetic permeability μ in $\mathrm{H\,m^{-1}}$,
- negligible displacement currents with respect to the electric current of free charges, $\boldsymbol{J}^{\mathrm{f}} \gg \frac{\partial \boldsymbol{D}}{\partial t}$,
- negligible electric polarization, $\boldsymbol{D} = \epsilon \boldsymbol{E}$, with electric permittivity ϵ in $\mathrm{F\,m^{-1}}$,
- and negligible free charges, $q^{\mathrm{f}} = 0$.

The magnetic permeability is described by $\mu = \mu_r \mu_0$, where μ_r is material-specific relative permeability and $\mu_0 \approx 4\pi \times 10^{-7} \mathrm{H\,m^{-1}}$ is magnetic permeability of vacuum. Similarly, the electric permittivity is given by $\epsilon = \epsilon_r \epsilon_0$, with ϵ_r material-specific relative permittivity and electric permittivity of vacuum $\epsilon_0 \approx 8.854 \times 10^{-12} \mathrm{F\,m^{-1}}$. An extensive discussion of this approximation is elsewhere [46, ch. 6]. We continue with the outcome of the following equations and aim for solving them,

$$\begin{aligned} \nabla \times \boldsymbol{E} &= -\frac{\partial \boldsymbol{B}}{\partial t} \,, \\ \nabla \cdot \boldsymbol{B} &= 0 \,, \\ \nabla \times \frac{\boldsymbol{B}}{\mu} &= \boldsymbol{j}^{\mathrm{f}} \,, \\ \nabla \cdot \boldsymbol{j}^{\mathrm{f}} &= 0 \,. \end{aligned} \tag{2}$$

Equation $(2)_{1,2}$ contains six unknown components of the vectors $\boldsymbol{B}$ and $\boldsymbol{E}$ described by four equations. Their solution is straightforward by using the ansatz functions[1]

$$\begin{aligned} \boldsymbol{B} &= \nabla \times \boldsymbol{A} \,, \\ \boldsymbol{E} &= -\frac{\partial \boldsymbol{A}}{\partial t} - \nabla V \,, \end{aligned} \tag{3}$$

where V is electric potential and $\boldsymbol{A}$ is magnetic (vector) potential. As usual, the current density and electric field are related through Ohm's law for isotropic moving media with velocity $\boldsymbol{v}$,

$$\boldsymbol{j}^{\mathrm{f}} = \sigma(\boldsymbol{E} + \boldsymbol{v} \times \boldsymbol{B}) \,, \tag{4}$$

with electric conductivity σ in $\mathrm{S\,m^{-1}}$. Following the argumentation of [47, p. 40], the influence of the velocity of mass $\boldsymbol{v}$ can be neglected if

$$|\boldsymbol{j}^{\mathrm{f}}| \gg |\sigma \boldsymbol{v} \times \boldsymbol{B}| \Rightarrow \left| \nabla \times \frac{\boldsymbol{B}}{\mu} \right| \gg |\sigma \boldsymbol{v} \times \boldsymbol{B}| \,. \tag{5}$$

Using the characteristic magnetic flux density, B, characteristic length, L_0, and velocity, v_0, this relation is expressed in terms of a so-called magnetic Reynolds number R_{m}:

$$\frac{1}{\mu} \frac{B}{L_0} \gg \sigma v_0 B \Rightarrow R_{\mathrm{m}} = \mu \sigma v_0 L_0 \ll 1 \,. \tag{6}$$

The characteristic length in high-frequency systems is not a geometrical dimension but the penetration depth during operation. With increasing Alternating Current (AC) frequencies, currents concentrate near the surface of a conductor due to eddy currents induced in its inner part by the currents themselves (cf. [48]). This effect is called *skin effect* and is more pronounced at higher frequencies. It is described by the so-called penetration or skin depth, δ, which is defined as the depth where the current density is reduced to $\frac{1}{e}$ (approximately 37 %) of the value on the conductor surface [48, p. 17f.]:

$$\delta = \sqrt{\frac{2}{\sigma \omega \mu}} \,. \tag{7}$$

In the present case, using the characteristic values of the melt domain from Table 2 and a frequency of $\omega = 2\pi f$, with $f = 13.5\,\mathrm{kHz}$, the penetration depth in Eq. (7)) reads $\delta = L_0 = 3\,\mathrm{mm}$, $R_{\mathrm{m}} = 7.8 \times 10^{-5} \ll 1$. Hence, Eq. (4) is simplified to

$$\boldsymbol{j}^{\mathrm{f}} = \sigma \boldsymbol{E} = \sigma \left(-\frac{\partial \boldsymbol{A}}{\partial t} - \nabla V \right) \,. \tag{8}$$

The electric current is generated in all electrically conducting materials within the magnetic field of the inductor. Within the coil, Ω_{coil}, we prescribe a source current density, $\boldsymbol{j}_{\mathrm{s}}$, and neglect the induction effects by setting the respective electrical conductivity to zero. Hence, we obtain

$$\boldsymbol{j}^{\mathrm{f}} = \begin{cases} \boldsymbol{j}^{\mathrm{c}} & \forall \boldsymbol{x} \in \Omega_{\mathrm{coil}} \\ \sigma \left(-\frac{\partial \boldsymbol{A}}{\partial t} - \nabla V \right) & \text{otherwise} \end{cases} \,. \tag{9}$$

By using all aforementioned simplifications, we obtain the governing equations [47, p. 41]

$$\begin{aligned} \nabla \times \left(\frac{1}{\mu} \nabla \times \boldsymbol{A} \right) &= \boldsymbol{j}^{\mathrm{f}} \,, \\ \nabla \cdot \left(-\sigma \frac{\partial \boldsymbol{A}}{\partial t} - \sigma \nabla V \right) &= 0 \,. \end{aligned} \tag{10}$$

[1] The information loss due to reduction of the number of equations leads to the so-called gauge freedom, which is discussed, e.g., in [42, p. 181f.]

In a time-harmonic system with sinusoidal source currents with a frequency of ω, all time-dependant quantities are described by using Euler's formula, e.g. $\boldsymbol{A}(t) = \hat{\boldsymbol{A}}\exp(\mathrm{i}\omega t)$, with $\hat{\boldsymbol{A}}$ complex-valued amplitude. In this way, we obtain

$$\begin{aligned}\nabla\times\left(\frac{1}{\mu}\nabla\times\hat{\boldsymbol{A}}\right) &= \begin{cases}\hat{\boldsymbol{j}}^{\mathrm{c}} & \forall\boldsymbol{x}\in\Omega_{\mathrm{coil}}\\ \sigma(-\mathrm{i}\omega\hat{\boldsymbol{A}}-\nabla\hat{V}) & \text{otherwise}\end{cases},\\ \nabla\cdot(-\mathrm{i}\sigma\omega\hat{\boldsymbol{A}}-\sigma\nabla\hat{V}) &= 0\end{aligned} \tag{11}$$

In the following, for the sake of notational simplicity, we omit the hat.

In the axisymmetric case with spatial coordinates (r,ϕ,z) and corresponding unit vectors $\boldsymbol{e}_r,\boldsymbol{e}_\phi,\boldsymbol{e}_z$, with an azimuthal current $\boldsymbol{j}^{\mathrm{f}} = j_\phi\boldsymbol{e}_\phi$, an additional simplification is possible. According to Eq. (2) and (9), the electric field and magnetic flux density are then reduced to

$$\begin{aligned}\boldsymbol{E} &= E_\phi\boldsymbol{e}_\phi\ ,\\ \boldsymbol{B} &= B_r\boldsymbol{e}_r + B_z\boldsymbol{e}_z\ .\end{aligned} \tag{12}$$

Consequently, the vector and scalar potential (Eq. (3)) are simplified to

$$\begin{aligned}\boldsymbol{A} &= A_\phi\boldsymbol{e}_\phi\ ,\\ \nabla V = \frac{\partial V}{\partial\phi} &\Rightarrow V = \text{const.}\quad \forall\boldsymbol{x}\in rz\text{-plane}\ ,\end{aligned} \tag{13}$$

which means that the system is fully described by the single remaining component of the vector potential A_ϕ. The field equation for A_ϕ reads

$$\nabla\times\left(\frac{1}{\mu}\nabla\times A_\phi\boldsymbol{e}_\phi\right) = \begin{cases}j_\phi^{\mathrm{c}}\boldsymbol{e}_\phi & \forall\boldsymbol{x}\in\Omega_{\mathrm{coil}}\\ -\mathrm{i}\omega\sigma A_\phi\boldsymbol{e}_\phi & \text{otherwise}\end{cases} \tag{14}$$

Within the cross-section of the induction coil, we assume a constant distribution of current density, j_ϕ^{c}.

The computational domain, Ω, is encapsulated by a steel vessel where for simplified modeling electromagnetic penetration and heating of the vessel are neglected. Therefore, homogeneous boundary condition,

$$A_\phi = 0 \qquad \forall\boldsymbol{x}\in\partial\Omega\ , \tag{15}$$

is used on the closure, $\partial\Omega$.

An electric current produces a so-called Joule heat that is given by [49, p. 59], [50, §286], [51]

$$h^{\mathrm{j}} = \boldsymbol{j}^{\mathrm{f}}\cdot\boldsymbol{E} = \frac{|\boldsymbol{j}^{\mathrm{f}}|^2}{\sigma}\ . \tag{16}$$

For the coupling of time-harmonic heating to the steady-state heat equation; the root-mean-square value of the current density is given by $\boldsymbol{j}^{\mathrm{f}}_{\mathrm{rms}} = \frac{\hat{\boldsymbol{j}}}{\sqrt{2}}$ for sinusoidal waves. Thus, we obtain

$$h^{\mathrm{j}}_{\mathrm{rms}} = \frac{|\hat{\boldsymbol{j}}|^2}{2\sigma} = \frac{\Re(\hat{\boldsymbol{j}})^2+\Im(\hat{\boldsymbol{j}})^2}{2\sigma} = \sigma\omega^2\frac{\Re(\hat{A}_\phi)^2+\Im(\hat{A}_\phi)^2}{2}\ . \tag{17}$$

3.2. Heat transfer

For computing temperature distribution transiently, We use the balance of internal energy, u (per unit mass) in $\mathrm{J\,kg^{-1}}$, as given by (cf. [37, Chap. 2], [52, Chap. 6], [42, Chap. 3],

$$\rho\frac{\mathrm{d}u}{\mathrm{d}t} + \nabla\cdot\boldsymbol{q} = h + \boldsymbol{\sigma}\cdot\cdot\nabla\boldsymbol{v}\ , \tag{18}$$

with[2] mass density ρ in $\mathrm{kg\,m^{-3}}$, heat flux $\boldsymbol{q}$ in $\mathrm{W\,m^{-2}}$, source term h in $\mathrm{W\,m^{-3}}$, Cauchy stress tensor $\boldsymbol{\sigma}$ in $\mathrm{N\,m^{-2}}$, and velocity $\boldsymbol{v}$ in $\mathrm{m\,s^{-1}}$.

For application in modeling of CZ growth, this equation can be further simplified under the following assumptions (cf. [42, Chap. 2]):

- low velocities, so that internal energy depends only on temperature T in K, and $\frac{\mathrm{d}u}{\mathrm{d}t} = c\frac{\mathrm{d}T}{\mathrm{d}t}$, with specific heat capacity[3] c in $\mathrm{J\,kg^{-1}\,K^{-1}}$,
- low internal friction compared to source $\boldsymbol{\sigma}\cdot\cdot\nabla\boldsymbol{v} \ll h$,
- using the definition of the total differential, $\frac{\mathrm{d}T}{\mathrm{d}t} = \frac{\partial T}{\partial t} + (\boldsymbol{v}\cdot\nabla)T$,
- Fourier's law of thermal conduction, $\boldsymbol{q} = -\kappa\nabla T$, with heat conductivity[4] κ in $\mathrm{W\,m^{-1}\,K^{-1}}$,

[2] The production term, $\boldsymbol{\sigma}\cdot\cdot\nabla\boldsymbol{v}$, is a scalar in units of a power density in index notation, $\sigma_{ij}v_{j,i}$ where comma means a partial space derivative and summation convention applies. Since stress is symmetric in this application, $\boldsymbol{\sigma}:\nabla\boldsymbol{v}$ is equivalent, $\sigma_{ji}v_{j,i}$.

[3] It is usually distinguished between specific heat capacity at constant pressure, c_p, and constant volume, c_v. Under the assumption of incompressible media applies $c_p = c_v$.

[4] In the case of isotropic materials κ is a scalar. In anisotropic materials, heat conduction can be described using the heat conductivity tensor $\boldsymbol{\kappa}$ [37, p. 330f.].

so that the so-called heat equation is obtained that describes the transport of heat by conduction and convection,

$$\rho c \left(\frac{\partial T}{\partial t} + (\boldsymbol{v} \cdot \nabla) T \right) - \nabla \cdot (\kappa \nabla T) = h \ , \tag{19}$$

In electromagnetically heated systems, the source term, $h = h^{\mathrm{j}}$, is given by the Joule heat (Eq. (16)/(17)). The heating of the coil itself, which is internally cooled with water and remains cold on its surface, is omitted.

The influence of the time-dependent terms can be estimated by the so-called Fourier number, Fo, which relates the heat conduction to the heat storage term using characteristic values:

$$\frac{|\nabla \cdot \kappa \nabla T|}{|\rho c \frac{\partial T}{\partial t}|} \Rightarrow \frac{\frac{1}{L_0} \kappa \frac{1}{L_0} T_0}{\rho c \frac{T_0}{t_0}} = \frac{\kappa t_0}{\rho c L_0^2} = Fo \ , \tag{20}$$

with characteristic length L_0, temperature T_0, and time t_0. With a sufficiently high Fourier number $Fo \gg 1$, which is, e.g., fulfilled regarding the motion of the crystal due to the low velocity upward pulling with a Fourier number of $Fo = 257 \gg 1$ computed using the characteristic values from Table 2, a steady state can be assumed and Eq. (19) is simplified to

$$\rho c (\boldsymbol{v} \cdot \nabla) T - \nabla \cdot (\kappa \nabla T) = h^{\mathrm{j}} \ . \tag{21}$$

The influence of the convective and conductive terms are analyzed by estimating their ratio that yields, expressed in terms of characteristic length L_0, velocity v_0, and temperature T_0, the so-called Peclet number Pe:

$$\frac{|\rho c (\boldsymbol{v} \cdot \nabla) T|}{|\nabla \cdot \kappa \nabla T|} \Rightarrow \frac{\rho c v_0 \frac{1}{L_0} T_0}{\frac{1}{L_0} \kappa \frac{1}{L_0} T_0} = \frac{\rho c L_0 v_0}{\kappa} = Pe \ , \tag{22}$$

with characteristic[5] length L_0, velocity v_0, and temperature T_0. In the case of $Pe \ll 1$, the convection term can be dropped, and Eq. (21) is further simplified to

$$-\nabla \cdot (\kappa \nabla T) = h^{\mathrm{j}} \ . \tag{23}$$

In the present system, using the values from Table 2, the Peclet number of the moving crystal is given by $Pe = 0.0039 \ll 1$ and, thus, convective heat transport may be neglected. In the gas domain $Pe = 18402 \gg 1$ and, thus, heat convection dominates over conduction. Instead of considering it explicitly through a computationally expensive gas flow model, the gas domain is excluded from the heat transfer model and the convective cooling is approximated through heat transfer coefficients (HTC) at the boundary conditions as described below. Within the melt, $Pe = 61$, heat convection modeling is required. A crude approximation is possible using an increased effective heat conductivity

$$\kappa_{\mathrm{eff}} = \kappa + \kappa_{\mathrm{conv}} \tag{24}$$

in Eq. (23), with the modeling parameter κ_{conv}. This approximation increases heat diffusion in order to accommodate the neglected convection. Indeed, this approach is not general and may only be applied if the velocity gradient and temperature gradient are aligned in parallel within the entire domain. Consequently, such a simplification in the presented model has to be treated with great care when investigating a local temperature field. In a global sense; however, regarding the total heat transfer between two surfaces, e.g., crucible-melt and crystal-melt interfaces, this approach may be a useful approximation that helps to reduce modeling complexity significantly. In the following, for the sake of notational simplicity, we use κ instead of κ_{eff}.

As justified with the aforementioned Peclet and Fourier numbers it is inadequate to use Eq. (23) for modeling of the gas domain. Therefore, the gas domain is excluded from the thermal model, and at the boundaries to the gas in Fig. 1, the convective cooling is modeled by

$$\boldsymbol{q}_{\mathrm{conv}} \cdot \boldsymbol{n} = \alpha (T - T_{\mathrm{ext}}) \ , \tag{25}$$

with the convective heat transfer coefficient, α, as an additional to-be-determined parameter. Furthermore, at boundaries, heat radiation is modeled by

$$\boldsymbol{q}_{\mathrm{rad}} \cdot \boldsymbol{n} = \sigma_{\mathrm{sb}} \epsilon (T^4 - T_{\mathrm{ext}}^4) \ , \tag{26}$$

with the Stefan–Boltzmann constant, $\sigma_{\mathrm{sb}} = 5.6704 \times 10^{-8}\,\mathrm{W/m^2K^4}$, emissivity, ϵ, and external (ambient) temperature, T_{ext}. Combination of Eq. (25) with (26) leads to the boundary condition:

$$-\kappa \nabla T \cdot \boldsymbol{n} = \alpha (T - T_{\mathrm{ext}}) + \sigma_{\mathrm{sb}} \epsilon (T^4 - T_{\mathrm{ext}}^4) \ . \tag{27}$$

[5] In some cases it may be required to use different characteristic values than for computation of the Fourier number (Eq. (20)). With the approximation of the characteristic time by $t_0 = \frac{L_0}{v_0}$ applied here the Peclet number is related to the Fourier number by $Pe = \frac{1}{Fo}$.

Due to the crystallization, latent heat is released at the interface between the solid crystal and the liquid melt. The crystallization process is described by the Stefan condition [53] that leads in steady-state to the additional interface condition

$$[\![\boldsymbol{q}]\!] \cdot \boldsymbol{n} = -L\rho_s v_p, \tag{28}$$

where $[\![\cdot]\!]$ denotes the difference of the values belonging to both phases on the interface. This jump is governed by the latent heat, $L = 59.6\,\mathrm{kJ/kg}$, the mass density of the solidified material, ρ_s, i.e. solid tin, and the local solidification velocity, v_p, which coincides with the upward pulling velocity of the crystal in steady state.

At the outside boundary of the water-cooled top and bottom axis, ambient temperature is set to T_{ext}.

3.3. Shape of the free surface

Owing to surface tension, the melt rises at the crystal, forming the so-called meniscus. Its shape is indispensable for crystal growth, as it influences the local temperature distribution in melt and crystal and, thus, the position of the solid/liquid interface as well as the growth angle, which is of great importance for the development of the crystal diameter.

The relation between surface tension, pressure, and curvature at every point on the free surface is given by the Young–Laplace equation:

$$p_2 - p_1 = -\gamma\left(\frac{1}{r_1} + \frac{1}{r_2}\right), \tag{29}$$

with interface pressure difference, $p_2 - p_1$, principal curvature radii r_1 and r_2 (see Fig. 2), and surface tension, γ, as a material parameter.

Under the assumption of constant pressure in the gas and hydrostatic pressure in the fluid, the interface pressure difference is given by $p_2 - p_1 = \rho g z$, with fluid density ρ, gravitational acceleration (specific force) g, and vertical position z. Under the assumption of a Cartesian 2D case with an infinitely extended fluid in the out-of-plane direction, the corresponding curvature radius $r_1 = \infty$. Under the additional assumption of constant surface tension Eq. (29) is solved analytically [54, §61] using the expression

$$r_2 = -\left(1 + \left(\frac{\mathrm{d}z}{\mathrm{d}x}\right)^{\frac{3}{2}}\right)\frac{\mathrm{d}^2 z}{\mathrm{d}x^2}\ , \tag{30}$$

with horizontal coordinate x, spanning from $x = 0$ at the wall (crystal) to the infinity, and vertical coordinate z with $z = 0$ at the surface level in infinite distance of the wall (see Fig. 2). The resulting surface shape solving the differential equation is then given by

$$\begin{aligned} x &= \lambda_c\left(\cosh^{-1}\left(\frac{2\lambda_c}{z}\right) - \cosh^{-1}\left(\frac{2\lambda_c}{h}\right)\right) - \lambda_c\left(\sqrt{4 - \frac{z^2}{\lambda_c^2}} - \sqrt{4 - \frac{h^2}{\lambda_c^2}}\right), \\ \lambda_c &= \sqrt{\frac{\gamma}{\rho g}}, \\ h &= \lambda_c\sqrt{2 - 2\sin(\beta)}. \end{aligned} \tag{31}$$

The substitute λ_c is also known as capillary constant; h is equal to the maximum rise of the fluid at the wall (see Fig. 2) and depends on the material-dependent wetting angle between fluid and wall β. A value of $\beta = 10°$ is measured for liquid tin from a closeup photograph in a growth experiment, a picture of this experiment together with the meniscus shape from Eq. (31) is shown in Fig. 2. Obviously, the assumption $r_1 = \infty$ is providing a reasonably accurate model of the meniscus shape as compared in the photograph. Although a certain deviation of the real surface shape is expected from the above equation, this closed-form solution is beneficial as it provides a simple yet in most cases sufficiently accurate approximation. An alternative implementation is conceivable via an approximation of the free surface shape as discussed, e.g., in [55].

4. Numerical modeling

4.1. Finite element formulation

A standard variational formulation is utilized in order to acquire the weak forms from the governing equations. Governing equations are utilized for electromagnetic potential in Eq. (14) and for temperature in Eq. (23) in order to generate weak forms and then solve them numerically by means of the finite element method [56]. The space discretization is employed for A_ϕ and T by spanning over nodal values after a triangulation of the computational domain, Ω, with its closure, $\partial\Omega$. This discrete representation of A_ϕ and T is never written in the same formulation as their analytical counterpart, so the same notation in the weak form is used. The solution space is Hilbertian–Sobolev, $\mathcal{H}^1$, on a triangulation τ, as follows:

$$\mathcal{V} = \left\{ \{A_\phi\} \in \mathcal{H}^1(\Omega) : \{A_\phi\}\big|_\tau \mathcal{P}_a(\tau)\ \forall\tau \in \mathcal{T} \wedge \{T\} \in \mathcal{H}^1(\Omega) : \{T\}\big|_\tau \mathcal{P}_b(\tau)\ \forall\tau \in \mathcal{T} \right\}\ . \tag{32}$$

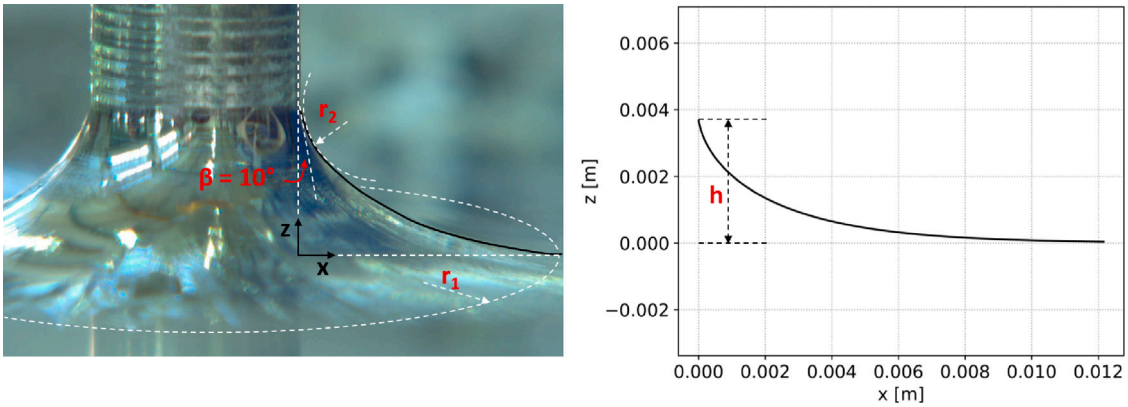

Fig. 2. Melt meniscus: picture from growth experiment including wetting angle and principal curvature radii (left), analytical shape under the assumption of a Cartesian 2D case (right).

Standard Lagrange elements are utilized over the triangulation $\mathcal{T}$ consisting of non-overlapping triangles, τ. Standard FEM elements of order $a = 1$ and $b = 1$, i.e. linear elements for both unknowns, are used. As known as the Galerkin approach [57], the same space is applied for their test functions, δA_ϕ and δT. The weak form of the magnetic potential reads

$$\int_\Omega \left(\frac{1}{\mu} (\nabla \times A_\phi \boldsymbol{e}_\phi) \cdot (\nabla \times \delta A_\phi \boldsymbol{e}_\phi) - j_\phi^{\mathrm{f}} \boldsymbol{e}_\phi \cdot \delta A_\phi \boldsymbol{e}_\phi \right) \mathrm{d}V = 0 \ . \tag{33}$$

As cylindrical coordinates for the axisymmetric problem are applied

$$\int_\Omega \left(\frac{1}{\mu} \left(\frac{\partial A_\phi}{\partial z} \boldsymbol{e}_r - \frac{1}{r} \frac{\partial r A_\phi}{\partial r} \boldsymbol{e}_z \right) \cdot \left(\frac{\partial \delta A_\phi}{\partial z} \boldsymbol{e}_r - \frac{1}{r} \frac{\partial r \delta A_\phi}{\partial r} \boldsymbol{e}_z \right) - j_\phi^{\mathrm{f}} \delta A_\phi \right) r \, \mathrm{d}r \, \mathrm{d}\phi \, \mathrm{d}z = 0 \ , \tag{34}$$

we obtain

$$\int_\Omega \left(\frac{1}{\mu} \frac{\partial A_\phi}{\partial z} \frac{\partial \delta A_\phi}{\partial z} + \frac{1}{\mu r^2} \frac{\partial r A_\phi}{\partial r} \frac{\partial r \delta A_\phi}{\partial r} \right) r \, \mathrm{d}r \, \mathrm{d}z + \int_{\Omega_{\mathrm{c}}} \left(\mathrm{i}\omega\sigma A_\phi \delta A_\phi \right) r \, \mathrm{d}r \, \mathrm{d}z - \int_{\Omega \setminus \Omega_{\mathrm{c}}} \left(j_\phi^{\mathrm{c}} \delta A_\phi \right) r \, \mathrm{d}r \, \mathrm{d}z = 0 \ , \tag{35}$$

where the integrand is constant in ϕ such that the integration $\int_\Omega \mathrm{d}\phi = 2\pi$ is canceled out of the equations.

Analogously, for T in Eqs. (23), (27) the weak form reads

$$\int_\Omega \left(\kappa \nabla T \cdot \nabla \delta T - \sigma\omega^2 \frac{(A_\phi)^2}{2} \delta T \right) \mathrm{d}V = - \int_{\Gamma_{\mathrm{r}}} \sigma_{\mathrm{sb}} \epsilon \left(T^4 - T_{\mathrm{ext}}^4 \right) \delta T \, \mathrm{d}A - \int_{\Gamma_{\mathrm{c}}} \alpha \left(T - T_{\mathrm{ext}} \right) \delta T \, \mathrm{d}A + \int_{\Gamma_{\mathrm{i}}} L \rho_{\mathrm{s}} v_{\mathrm{p}} \delta T \, \mathrm{d}A \ . \tag{36}$$

In the case of cylindrical coordinates, for the left-hand side of Eq. (36), we acquire

$$\int_\Omega \left(\kappa \left(\frac{\partial T}{\partial r} \boldsymbol{e}_r + \frac{\partial T}{\partial z} \boldsymbol{e}_z \right) \cdot \left(\frac{\partial \delta T}{\partial r} \boldsymbol{e}_r + \frac{\partial \delta T}{\partial z} \boldsymbol{e}_z \right) - \sigma\omega^2 \frac{(A_\phi)^2}{2} \delta T \right) r \, \mathrm{d}r \, \mathrm{d}\phi \, \mathrm{d}z = \int_\Omega \left(\kappa \frac{\partial T}{\partial r} \frac{\partial \delta T}{\partial r} + \frac{\partial T}{\partial z} \frac{\partial \delta T}{\partial z} - \sigma\omega^2 \frac{(A_\phi)^2}{2} \delta T \right) r \, \mathrm{d}r \, \mathrm{d}\phi \, \mathrm{d}z \ . \tag{37}$$

For evaluation of the right-hand side of Eq. (36), the infinitesimal area element described by $\mathrm{d}A = \boldsymbol{n} \cdot (\mathrm{d}z \, \mathrm{d}\phi \boldsymbol{e}_r + \mathrm{d}r \, \mathrm{d}\phi \boldsymbol{e}_z)$ using a projection on the surface normal, $\boldsymbol{n}$. Considering that the integrand is constant in $\mathrm{d}\phi$ the projection $\mathrm{d}\tilde{A} = \boldsymbol{n} \cdot (\mathrm{d}z \boldsymbol{e}_r + \mathrm{d}r \boldsymbol{e}_z)$, we obtain

$$\int_\Omega \left(\kappa \frac{\partial T}{\partial r} \frac{\partial \delta T}{\partial r} + \frac{\partial T}{\partial z} \frac{\partial \delta T}{\partial z} - \sigma\omega^2 \frac{(A_\phi)^2}{2} \delta T \right) r \, \mathrm{d}r \, \mathrm{d}z = - \int_{\Gamma_{\mathrm{r}}} \sigma_{\mathrm{sb}} \epsilon \left(T^4 - T_{\mathrm{ext}}^4 \right) \delta T r \, \mathrm{d}\tilde{A} - \int_{\Gamma_{\mathrm{c}}} \alpha \left(T - T_{\mathrm{ext}} \right) \delta T r \, \mathrm{d}\tilde{A} + \int_{\Gamma_{\mathrm{i}}} L \rho_{\mathrm{s}} v_{\mathrm{p}} \delta T r \, \mathrm{d}\tilde{A} \ . \tag{38}$$

4.2. Mesh update

Isotherm of the melting temperature, Γ_{i}^n, is employed for altering the geometry. In this way, a sharp interface between solid and liquid phases is obtained. In order to determine the isothermal, cells (finite elements) $\mathbb{C} \in \mathbb{T}_h^n$ with both vertices of larger and smaller temperature than the melting temperature are marked. Since the temperature is represented by first-order finite elements, the temperature distribution within the cell is linear. Hence, the location of the melting temperature on the edge between the opposing vertices is immediately computed as demonstrated in Fig. 3. Consequently, the isothermal is a piecewise linear graph $\boldsymbol{\Phi}$.

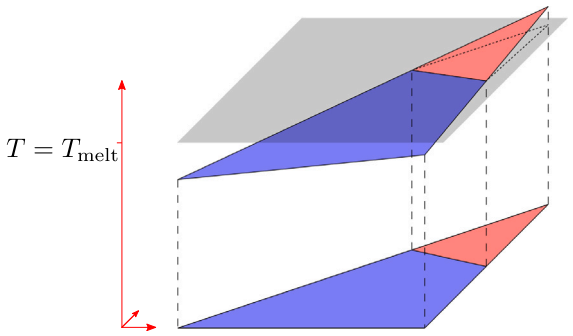

Fig. 3. Projection of isotherm onto the geometry. The intersection of the isotherm T_{melt} (grey) with the linear temperature field is projected on the cell. (For interpretation of the references to color in this figure legend, the reader is referred to the web version of this article.)

By parameterizing the isothermal over the length, the graph is represented as

$$\boldsymbol{\Phi}^{n+1} : [0,1] \to \Gamma_{\text{i}}^{n+1}. \tag{39}$$

With this representation, it is possible to define a mapping from the old interface to the new one through

$$\Gamma_{\text{i}}^{n+1} = \boldsymbol{\Phi}^{n+1}\left((\boldsymbol{\Phi}^{n})^{-1}(\Gamma_{\text{i}}^{n})\right), \tag{40}$$

which ensures that the spacing of the nodes on the isotherm is maintained in terms of the parametrization, even in the case of large interface deflections. It should be noted that the parametrization of the isotherm is not strictly required; in the case of small interface deflections, a simple mesh deformation in the vertical direction would be sufficient. For obtaining a global mesh deformation the harmonic extension of (40) is chosen. This approach introduces an auxiliary problem for the mesh movement, where the global mesh deformation $\boldsymbol{u}$ is obtained as the solution to

$$\begin{aligned} -\Delta\boldsymbol{u} &= 0 && \text{in } \Omega, \\ \boldsymbol{u}(\boldsymbol{x}) &= \boldsymbol{\Phi}^{n+1}\left((\boldsymbol{\Phi}^{n})^{-1}(\boldsymbol{x})\right) - \boldsymbol{x} && \text{for } \boldsymbol{x} \in \Gamma_{\text{i}}^{n}, \\ \boldsymbol{u}\cdot\boldsymbol{n} &= 0 && \text{on } \Gamma_{\text{sym}}, \\ \boldsymbol{u} &= 0 && \text{on } \partial\Omega \setminus \Gamma_{\text{sym}}. \end{aligned} \tag{41}$$

This formulation slightly deviates from the usual harmonic extension allowing a mesh motion in the vertical direction on the symmetry axis. The finite element discretization of the auxiliary problem (41) reads

$$\int_{\Omega} \nabla\boldsymbol{u} \cdot\cdot \nabla\delta\boldsymbol{u}\,\mathrm{d}V = 0\,, \tag{42}$$

where we represent trial and test functions from a standard linear space. This global mesh movement is drawn in Fig. 4.

4.3. Solution procedure

Different methodologies are possible leading to a combination of solving weak forms for magnetic potential, temperature, and mesh motion. We have implemented the procedure by following Algorithm 1. Note that the Joule heating term in Eq. (23) is scaled in order to obtain the correct temperature level, i.e. the melting temperature at the contact point between solid, liquid, and gas phase on the surface of melt/crystal (triple point). Due to quadratic dependency between Joule heating and source current density, j_{ϕ}^{c}, this is equal to scaling inductor current as done in process control but computationally more efficient because the electromagnetic computation has not to be repeated (in the present case with constant material properties). It makes the heating current a result of the simulation:

$$I_{\text{ind}} = \sqrt{c} I_0, \tag{43}$$

with c obtained Joule heat scaling and I_0 inductor current applied in the computation of A_{ϕ}.

The solution procedure is implemented in Python using dolfinx v0.5.2 [58]. To achieve the simplest possible implementation, all equations are solved in the complex domain, although this setup is only necessary for Eq. (33). The corresponding code is provided in [59].

5. Verification

For verification of the induction heating model, a cylinder in an infinitely long coil was investigated. The reference geometry of the simulation is visualized in Fig. 5. It consists of a graphite cylinder and a solenoid coil model with a solid volume of constant current density, surrounded by air. A zero-gradient condition $\frac{\partial A_{\phi}}{\partial \boldsymbol{n}} = 0$ is applied at the top and bottom boundaries of the finite

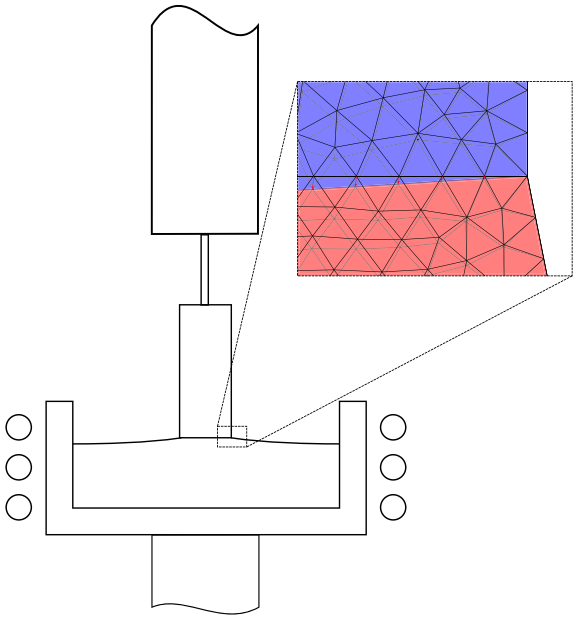

Fig. 4. Mesh deformation at crystallization front. Its shape is changed to fit the crystallization front where $T < T_{\text{melt}}$ (blue) and melt where $T > T_{\text{melt}}$ (red). (For interpretation of the references to color in this figure legend, the reader is referred to the web version of this article.)

Algorithm 1 Iterative solving process

Set initial mesh $\mathbb{T}_h^0$ and initial isothermal $\boldsymbol{\Phi}^0$.
for $n = 0, 1, 2, \ldots$ **do**
  Compute magnetic potential A_ϕ.
  Compute temperature field T and scale Joule heating term to match temperature on triple point.
  if $\int_{\Gamma_{\text{i}}^n} (T - T_{\text{melt}})^2 \mathrm{d}V < TOL$ **then**
    break
  end if
  Interpolate isothermal graph $\boldsymbol{\Phi}^{n+1}$.
  Compute new melting interface as

$$\Gamma_{\text{i}}^{n+1} = \boldsymbol{\Phi}^{n+1}\left((\boldsymbol{\Phi}^n)^{-1}(\Gamma_{\text{i}}^n)\right).$$

  Solve mesh movement equation for mesh deformation $\boldsymbol{u}$.
  Obtain new mesh $\mathbb{T}_h^{n+1}$ from mesh deformation $\boldsymbol{u}$.
end for

computation domain to model the infinite extension in this direction. As far-away boundary conditions, at the outside boundary of the surrounding air, $A_\phi = 0$ is set. To achieve a magnetic flux density similar to the experiment described in Section 2, a source current density of $j_\phi^{\text{c}} = 600\,\text{kA}\,\text{m}^{-2}$ with a frequency of $f = 13.5\,\text{kHz}$ is set in the volume of the coil. The materials are non-magnetic with an electric conductivity of $\sigma = 58.8\,\text{kS}\,\text{m}^{-1}$ in the graphite. In the coil, zero electric conductivity is set to avoid self-induction. Air is an isolator. Temperature distribution in the cylinder is modeled with zero-gradient condition $\frac{\partial T}{\partial \boldsymbol{n}} = 0$ at the top and bottom boundaries; convective and radiate cooling (to ambient) (Eq. (27)) at the surface using a heat conductivity of $65\,\text{W}\,\text{m}^{-1}\,\text{K}^{-1}$, an emissivity of 0.7, and a heat transfer coefficient of $10\,\text{W}\,\text{m}^{-2}\,\text{K}^{-1}$ with an ambient temperature of $300\,\text{K}$.

5.1. Analytical solution

Under the assumptions stated above the induction heating problem is reduced to a quasi-1D problem, for which (among other quantities) the induced heat and the resulting surface temperature can be computed analytically.

Assuming a time-harmonic (sinusoidal) electric current, the induced magnetic flux density $\boldsymbol{B}$ is given by the following Maxwell's equations (cf. [49, Ch. 6.2]):

$$\begin{aligned} \nabla \times \frac{\boldsymbol{B}}{\mu_0} &= \sigma \boldsymbol{E} \\ \nabla \times \boldsymbol{E} &= -\mathrm{i}\omega \boldsymbol{B}\,. \end{aligned} \tag{44}$$

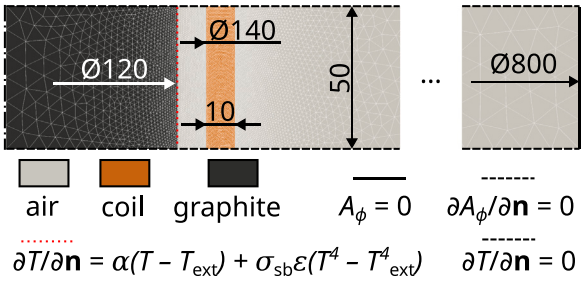

Fig. 5. Simulation setup with mesh, materials and dimensions (in mm). The symmetry axis is on the left side.

In the case of an axisymmetric geometry with infinite extension in the axial direction, thus without dependence on the axial coordinate, only B_z and E_ϕ are non-zero. Therefore, the system of equations is further simplified and combined into a single equation:

$$\begin{aligned} E_\phi &= -\frac{1}{\mu_0\sigma}\frac{\partial B_z}{\partial r}\,, \\ \frac{\partial E_\phi}{\partial r} + \frac{E_\phi}{r} &= -\mathrm{i}\omega B_z\,, \\ \Rightarrow \frac{\partial^2 B_z}{\partial r^2} + \frac{1}{r}\frac{\partial B_z}{\partial r} &- \mathrm{i}\mu_0\sigma\omega B_z = 0\,. \end{aligned} \tag{45}$$

The magnetic flux density inside an empty (infinitely) long coil is given by [49, Eq. (6.1)]

$$B_{z,\mathrm{gap}} = \frac{NI}{\mu_0 \ell} \tag{46}$$

with coil length, ℓ, number of windings N, and current I. With the latter, Eq. (45) is solved analytically [49, Eq. (6.9)], leading to the following current density distribution within the cylinder:

$$\begin{aligned} j_{\mathrm{ana}} &= \frac{\sqrt{-2\mathrm{i}}\; B_{z,\mathrm{gap}}}{\mu_0\delta}\frac{J_1\left(\frac{\sqrt{-2\mathrm{i}}\; r}{\delta}\right)}{J_0\left(\frac{\sqrt{-2\mathrm{i}}\; r_e}{\delta}\right)}\,, \\ \delta &= \sqrt{\frac{2}{\mu_0\sigma\omega}}\,, \end{aligned} \tag{47}$$

with Bessel functions of zero and first order, J_0 and J_1, respectively, outer radius of the graphite cylinder, r_e, and penetration depth, δ. The mean Joule's heat production is given by Eq. (17), as follows:

$$h_{\mathrm{j,mean}} = \frac{|j_{\mathrm{ana}}|^2}{2\sigma}\,, \tag{48}$$

in the present case with sinusoidal current. It was evaluated in a `Python` script using the package *SciPy* [60].

In the case of a steady-state, the total induced power P_{ind} is dissipated fully across the boundaries with convective and radiative heat transfer (Eq. (27)), thus,

$$\begin{aligned} &\int_\Omega h^{\mathrm{j}}_{\mathrm{rms}}\mathrm{d}V = P_{\mathrm{ind}} = \int_\Gamma \Big(\alpha(T_{\mathrm{surf.}} - T_{\mathrm{ext}}) + \sigma_{\mathrm{sb}}\epsilon(T^4_{\mathrm{surf.}} - T^4_{\mathrm{ext}})\Big)\mathrm{d}A \\ \Leftrightarrow\; &2\pi\ell\int_0^{r_e} h^{\mathrm{j}}_{\mathrm{rms}} r\mathrm{d}r = 2\pi r_e\ell\left(\alpha(T_{\mathrm{surf.}} - T_{\mathrm{ext}}) + \sigma_{\mathrm{sb}}\epsilon(T^4_{\mathrm{surf.}} - T^4_{\mathrm{ext}})\right), \end{aligned} \tag{49}$$

with length of the considered cylinder section ℓ. The latter is solved symbolically for the surface temperature T_{surf} by using the package *SymPy* [61], for details, it is referred to Appendix A.

5.2. Numerical solution

To ensure a converged solution, three meshes of different resolutions, all created with Gmsh 4.10.0 [62], as shown in Table 3 and visualized Fig. 5 for $h_{\max} = 10\,\mathrm{mm}$ were employed. The resulting distribution of Joule heat inside the cylinder is visualized over the radius in Fig. 6. Adequate match is observed between the analytical and numerical solution with less than 1% relative error in each location; however, the error is almost independent of the mesh size, and convergence towards the analytical value cannot be seen. Correspondingly, an almost constant error in surface temperature of approximately 0.29% is obtained (see Table 3).

The radius of the outside boundary (where $A_\phi = 0$) is found to be the main reason for the deviation from the analytical solution. Simulation of three different radii, namely 400 mm, 800 mm and 1600 mm for the mesh size of $h_{\max} = 10\,\mathrm{mm}$ are performed for further investigation; the resulting errors in Joule heat and temperature at the cylinder surface are visualized in Fig. 7. Convergence towards the analytical solution with increasing boundary distance can be seen, with a minimum error in the Joule heating of 0.27% and temperature of 0.07%.

Table 3
Mesh properties and resulting surface temperature. The analytically computed temperature is $T_{ana} = 719.682\,K$.

Max. element size, h_{max}	Min. element size, h_{min}	Number of elements	Comp. surface temperature	Relative error
10.0 mm	0.5 mm	16 225	717.629 K	0.2853%
5.0 mm	0.25 mm	64 346	717.630 K	0.2851%
2.5 mm	0.125 mm	255 473	717.631 K	0.2850%

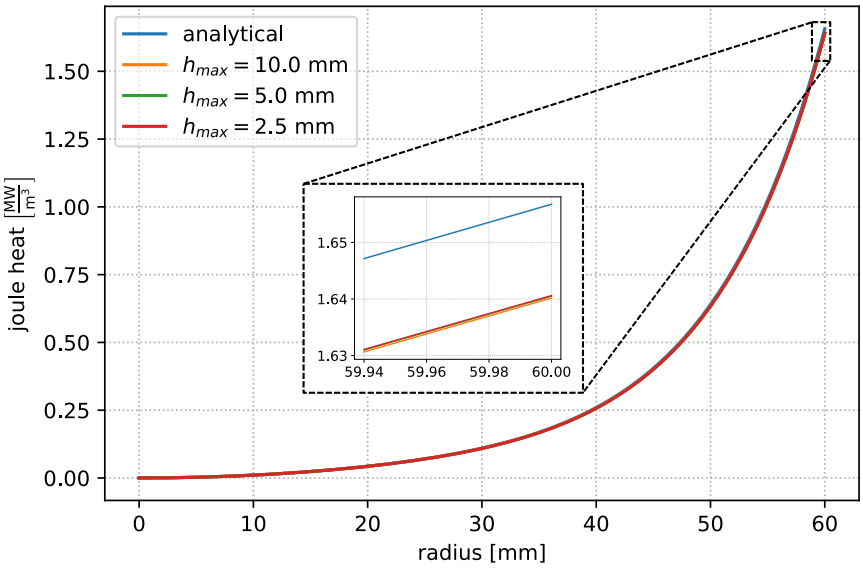

Fig. 6. Verification: influence of mesh size on induced Joule heat. The maximum deviation at the outer radius is between 1% (coarse mesh) and 0.95% (fine mesh).

Varying the coil thickness, which is 10 mm in the reference case, shows only an indirect influence on the simulation results: if the outer boundary radius is constant, a thicker coil reduces the distance between coil and boundary and, thus, deviation from the analytical solution increases. If the ratio between coil and boundary radius is maintained, no significant difference is detected.

In summary, a good agreement with the analytical solution was observed. By choosing the mesh size of $h_{max} = 10\,mm/h_{min} = 0.5\,mm$ and modeling the far-away conditions more than 10 times of the outer coil radius[6], the numerical solution delivers a relative error in the production term less than 0.3% and absolute error in surface temperature of 0.5 K. The implementation of the induction heating is considered verified in a case similar to the experiment.

6. Comparison to experimental results

In this section, the model is compared to experimental results to validate that the simplifying assumptions discussed in Section 3 are adequate and to estimate the modeling accuracy.

6.1. Setup

A steady-state experiment performed in the model growth furnace described in Section 2 is considered. A crystal equipped with three thermocouples at different vertical positions is attached to the melt which is controlled to remain at a given temperature. After homogenization, temperature and current are recorded.

An overview of the furnace dimensions, the positioning of the temperature sensors, the different materials and the mesh applied in the numerical simulation is given in Fig. 8; corresponding material properties are listed in Table 1. The remaining modeling parameters, i.e. the heat transfer coefficients at crystal, crucible, and melt surface as well as the effective heat conductivity of the melt, cannot be determined apriori and require empirical equations or dedicated experiments.

In a previous work [30], a crystal growth model using the finite element software Elmer has been validated using the same model experiment. There, HTC at crystal surface has been determined through crystal temperature measurements, HTC of crucible and melt have been determined based on the global power balance, and effective heat conductivity of the melt has been determined based on crystal diameter predictions. Repeating these complex calculation series and analyses would not add much value to the

[6] This is not relevant for the simulation of the crystal growth process, where the coil is surrounded by a steel vessel.

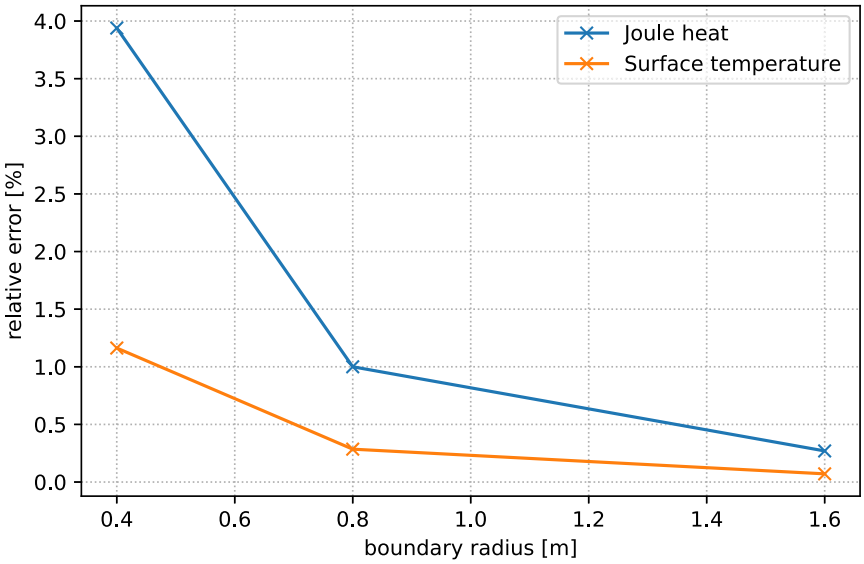

Fig. 7. Verification: influence of boundary radius on relative error in surface temperature.

present model. Therefore, it is assumed that these modeling parameters are the same for both models and HTC of $\alpha = 10\,\mathrm{W\,m^{-2}\,K^{-1}}$ on the surfaces of crystal, crucible and melt and effective heat conductivity of $\kappa_{\mathrm{eff}} = 62\,\mathrm{W\,m^{-1}\,K^{-1}}$ in the melt are adopted. The only difference between both models is the lack of surface-to-surface radiation modeling, which should not lead to significant changes in the aforementioned modeling parameters.

Mesh convergence was studied using three meshes consisting of 9 744, 33 979, 126 772 elements, analyzing the influence on required inductor current. The reference mesh consisting of 33 979 elements is found to have a sufficient accuracy, see Appendix B.

6.2. Verification and validation

Five mesh movement iterations were required to compute the shape of the crystallization interface with an integral tolerance of 10^{-10} m; the resulting temperature, Joule heating and magnetic flux density contour lines including the deformed mesh are shown in Fig. 9. The highest temperature of approximately 240 °C is reached in the crucible and melt. In the crystal, seed and insulation, there are steep temperature gradients while the adapter, bottom- and top axes remain cold with temperatures below 45 °C. Owing to the position and coil geometry, the magnetic flux density is strongest next to the crucible, yet penetrates into the melt as the penetration depth (Eq. (7)) in the crucible of 17.9 mm is greater than the wall thickness of 10 mm. Consequently, the maximum induced heat in the crucible of $0.75\,\mathrm{MW\,m^{-3}}$ is exceeded by the Joule heating in the melt of up to $1.95\,\mathrm{MW\,m^{-3}}$. The mesh at the crystallization front has been moved toward the melt by a maximum of 0.36 mm on the symmetry axis and fits the contour line of the crystallization front well; an adequate mesh quality without strongly deformed cells is preserved.

Comparison with experimental data and simulation using the model from [30] is compiled in Table 4. Similar results as with [30] were obtained, with differences in temperature of maximum 2.1 K in the crystal at the top position, 0.2 K in the melt, and 0.4 K in the crucible, and in heating current of 3 %. The obtained temperature values within the crystal match those from the experiment well, with a maximum deviation of 2 K in the mid position. In crucible and melt there are higher deviations of approximately 4 K, and the predicted heating current of 202.8 A, that is required to reach the melting temperature at the triple point, exceeds the value from the experiment by 22%.

Deviations in radiation modeling between the present model and [30] is obviously of minor influence and the assumed reason for the obtained small difference between the models. The good agreement between simulation and experiment in the crystal temperature can be attributed to accurate HTC at the crystal, deviations in melt and crucible temperature to inaccuracies in the simplified melt convection model based on κ_{eff}, and deviations in heating current to inaccuracies in geometry modeling and material properties. For an extensive discussion it is referred to [30].

7. Conclusion

A steady-state 2D model for Czochralski crystal growth has been developed and implemented in the open-source FEM software FEniCSx. The implementation includes heat generation by induction heating, heat conduction in solids, latent heat release, and mesh movement to match the solid–liquid isotherm of the crystallization interface. Melt convection is approximated with an effective heat conductivity; gas convection and radiation cooling are modeled using HTCs and an idealized-grey radiation-to-ambient approaches, respectively.

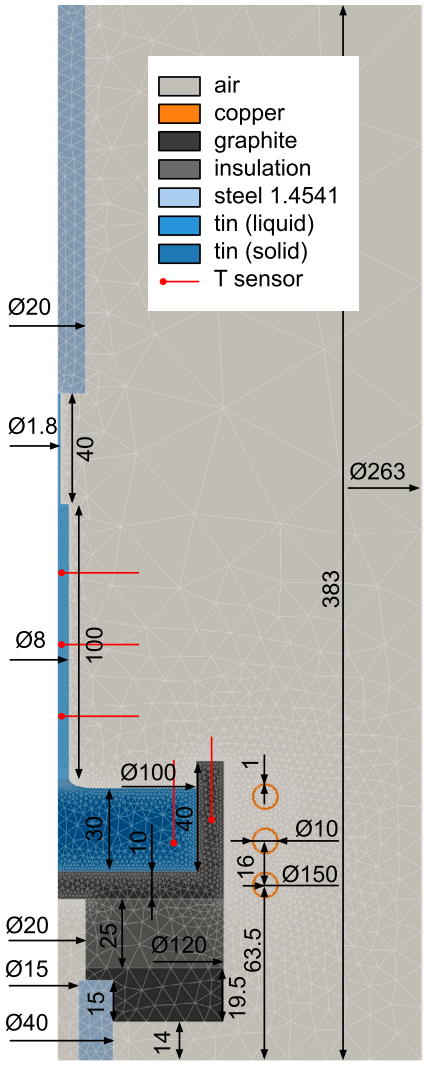

Fig. 8. Simulation setup with mesh, materials, dimensions, and measuring points.

Table 4
Comparison between simulation with the new model, simulation with the model from [30], and experiment at selected positions (with respect to crystal length ℓ).

Sensor	Simulation	Simulation [30]	Experiment
Temperature crystal bottom ($\ell/4$)	194.5 °C	195.5 °C	194.5 °C
Temperature crystal middle ($\ell/2$)	168.1 °C	169.7 °C	170.1 °C
Temperature crystal top ($3\ell/4$)	150.9 °C	153.0 °C	151.0 °C
Temperature melt	240.2 °C	240.0 °C	236 °C to 236.2 °C
Temperature crucible	240.4 °C	240.0 °C	235.5 °C to 236.1 °C
Heating current	202.8 A	208.1 A	166.2 A

Finite element formulation of the governing equations has been derived from general physical laws; all simplifying assumptions have been discussed and justified. The induction heating model has been verified against analytical solution for a cylinder placed inside a long coil. The full model has been compared to temperature and current measurements from a model experiment with tin and simulation using an alternative model [30]. Values determined in [30] were applied for the HTC of crystal, melt and crucible and the effective heat conductivity of the melt. Similar results as in [30] were obtained considering deviations between simulation and experiment in crystal temperature and inductor current, even though a superior heat radiation model considering surface-to-surface heat exchange was applied in [30]. The good agreement between the two models can be explained by the relatively low influence of heat radiation compared to convective cooling at the present temperature level in the model experiment with tin of 232 °C melting

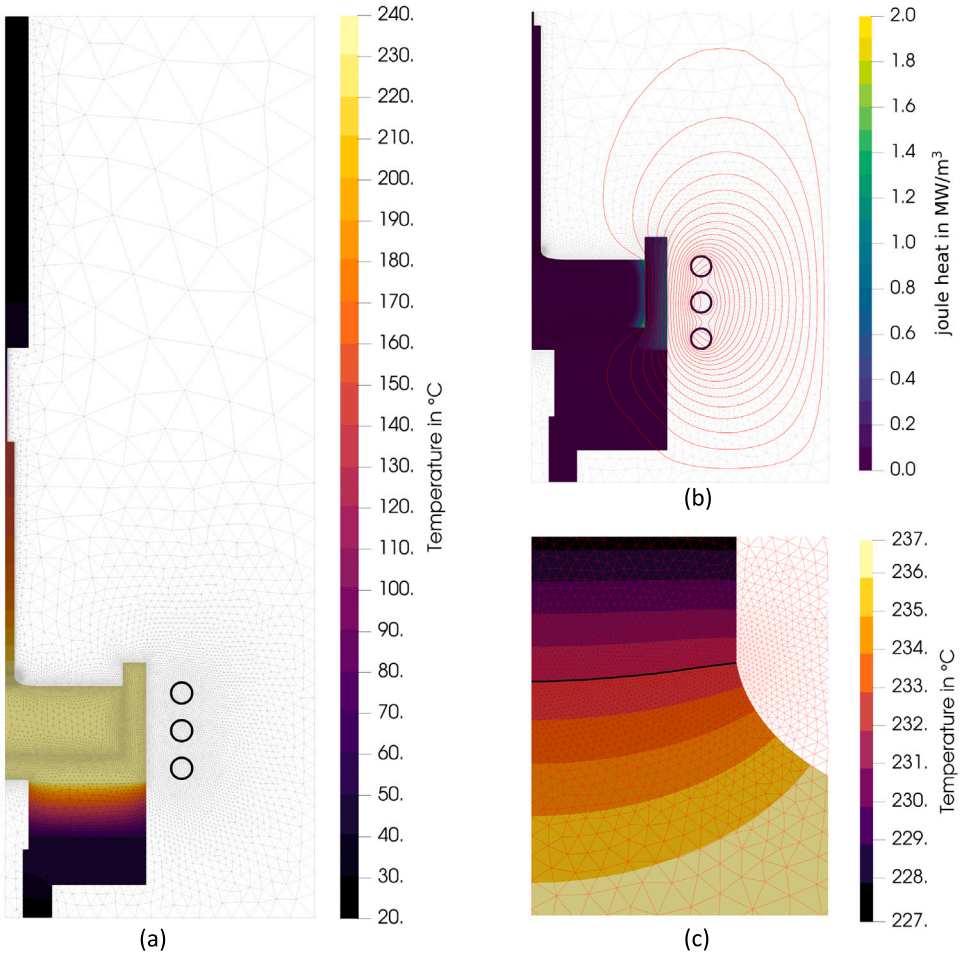

Fig. 9. Validation simulation result: (a) global temperature distribution, (b) Joule heating and magnetic flux density contour lines, (c) local temperature and deformed mesh at crystal-melt interface.

point. The overall agreement with the experiment is convincing, and a deviation of less than 4 K between simulation and experiment is observed in the crystal, crucible, and melt temperature. Melt convection modeling with effective heat conductivity is the assumed reason for this deviation; it requires careful adjustment for each specific application that was not performed here. The heating current in simulation is 22.2 % higher than in the experiment, which is assumed to be due to inaccuracies in geometry modeling and material parameters.

The implementation of the crystal growth model in FEniCSx using Python offers great advantages in terms of simplicity and readability, as it remains very close to the mathematical formulation but still provides access to the underlying data structures. Further developments of the model could focus on implementing temperature-dependent material parameters, surface-to-surface radiation, mesh movement with higher-order elements, the integration or coupling of a flow simulation, or the transient computation of the crystal diameter evolution.

CRediT authorship contribution statement

Arved Wintzer: Writing – original draft, Visualization, Software, Methodology, Investigation, Data curation. **Bilen Emek Abali:** Writing – review & editing, Software, Methodology, Investigation, Formal analysis. **Kaspars Dadzis:** Writing – review & editing, Supervision, Funding acquisition, Formal analysis, Conceptualization.

Declaration of competing interest

The authors declare that they have no known competing financial interests or personal relationships that could have appeared to influence the work reported in this paper.

Table 5
Results of mesh convergence study.

	$h_{max} = 52.6$ mm	$h_{max} = 26.3$ mm	$h_{max} = 13.15$ mm
Heating current	203.4 A	202.8 A	202.7 A
Crucible temperature	240.4 °C	240.4 °C	240.4 °C

Acknowledgments

Max Schröder (formerly IKZ) is gratefully acknowledged for supporting model implementation in FEniCS and description of the numerical model. This project has received funding from the European Research Council (ERC) under the European Union's Horizon 2020 research and innovation programme (grant agreement No 851768).

Appendix A. Cylinder surface temperature

The surface temperature of the cylinder is given by

$$T_{\text{surf.}} = \frac{\sqrt{6}\left(-\sqrt[4]{\pi}\sqrt[4]{\ell}\sqrt[4]{r_e}\sqrt{\sqrt[3]{12}a^{\frac{2}{3}} - b} + \sqrt{\frac{12\sqrt{6}\pi^{\frac{5}{4}}\sqrt{a}\alpha\ell^{\frac{5}{4}}r_e^{\frac{5}{4}} - \sqrt{\pi}\sqrt{\ell}\sqrt{r_e}\left(\sqrt[3]{12}a^{\frac{2}{3}} - b\right)^{\frac{3}{2}}}{\sqrt{\sqrt[3]{12}a^{\frac{2}{3}} - b}}}\right)}{12\sqrt{\pi}\sqrt[6]{a}\sqrt{\ell}\sqrt[3]{\epsilon}\sqrt{r_e}\sqrt[3]{\sigma_{\text{sb}}}}, \tag{50}$$

$$a = 9\pi^{\frac{3}{2}}\alpha^2\ell^{\frac{3}{2}}r_e^{\frac{3}{2}} + \sqrt{3}\sqrt{27\pi^3\alpha^4\ell^3r_e^3 + 32\epsilon\sigma_{\text{sb}}\left(P_{\text{ind}} + 2\pi T_{\text{ext}}^4\ell\epsilon r_e\sigma_{\text{sb}} + 2\pi T_{\text{ext}}\alpha\ell r_e\right)^3},$$

$$b = 4\cdot\sqrt[3]{18}\sqrt[3]{\epsilon}\sqrt[3]{\sigma_{\text{sb}}}\left(P_{\text{ind}} + 2\pi T_{\text{ext}}^4\ell\epsilon r_e\sigma_{\text{sb}} + 2\pi T_{\text{ext}}\alpha\ell r_e\right).$$

The source code for the computation of this solution with simpy [63] is provided in [59].

Appendix B. Mesh convergence

Mesh convergence is studied using three meshes consisting of 9744/33979/126772 elements generated with a Gmsh using the maximum mesh sizes $h_{max} = 52.6/26.3/13.15$ mm. The resulting inductor currents and crucible temperatures are listed in Table 5. It can be seen that there is a slight grid dependency of the inductor current, while the crucible temperature is mesh-independent. The mesh consisting of 33979 elements is selected for the validation study.

Data availability

Publicly available in git repository.

References

[1] D. Arndt, W. Bangerth, D. Davydov, T. Heister, L. Heltai, M. Kronbichler, M. Maier, J.-P. Pelteret, B. Turcksin, D. Wells, The deal.II finite element library: Design, features, and insights, Comput. Math. Appl. 81 (2021) 407–422.
[2] P.R. Schunk, R.R. Rao, Multicomponent two-phase flows with interphase mass and momentum transport, Int. J. Numer. Meth. Fluids. 18 (1994) 821–842.
[3] M.S. Alnæs, A. Logg, K.B. Ølgaard, M.E. Rognes, G.N. Wells, Unified form language: A domain-specific language for weak formulations of partial differential equations, ACM Trans. Math. Software 40 (2) (2014) 9:1–9:37.
[4] P. Dular, C. Geuzaine, F. Henrotte, W. Legros, A general environment for the treatment of discrete problems and its application to the finite element method, IEEE Trans. Magn. 34 (5) (1998) 3395–3398.
[5] G. Giudicelli, A. Lindsay, L. Harbour, C. Icenhour, M. Li, J.E. Hansel, P. German, P. Behne, O. Marin, R.H. Stogner, J.M. Miller, D. Schwen, Y. Wang, L. Munday, S. Schunert, B.W. Spencer, D. Yushu, A. Recuero, Z.M. Prince, M. Nezdyur, T. Hu, Y. Miao, Y.S. Jung, C. Matthews, A. Novak, B. Langley, T. Truster, N. Nobre, B. Alger, D. Andrš, F. Kong, R. Carlsen, A.E. Slaughter, J.W. Peterson, D. Gaston, C. Permann, 3.0 - MOOSE: Enabling massively parallel multiphysics simulations, SoftwareX 26 (2024) 101690.
[6] M. Malinen, P. Råback, Elmer finite element solver for multiphysics and multiscale problems, in: I. Kondov, G. Sutmann (Eds.), Multiscale Modelling Methods for Applications in Material Science.
[7] H.G. Weller, G. Tabor, H. Jasak, C. Fureby, A tensorial approach to computational continuum mechanics using object-oriented techniques, Comput. Phys. 12 (1998) 821–842.
[8] T.D. Economon, F. Palacios, S.R. Copeland, T.W. Lukaczyk, J.J. Alonso, SU2: An open-source suite for multiphysics simulation and design, AIAA J. 54 (3) (2015) 828–846.
[9] B.E. Abali, F. Aldakheel, T.I. Zohdi, Multiphysics computation of thermomechanical fatigue in electronics under electrical loading, in: Current Trends and Open Problems in Computational Mechanics, Springer, 2022, pp. 1–14.
[10] C.-V. Ince, A. Chugreeva, C. Böhm, F. Aldakheel, J. Uhe, P. Wriggers, B.-A. Behrens, A. Raatz, A design concept of active cooling for tailored forming workpieces during induction heating, Prod. Eng. 15 (2021) 177–186.
[11] F. Aldakheel, C. Soyarslan, H.S. Palanisamy, E.S. Elsayed, Machine learning aided multiscale magnetostatics, Mech. Mater. 184 (2023) 104726.

[12] U.T. Baler, A.F. Okyar, B.E. Abali, Digital twin of surface acoustic wave transceivers for a computational design of an optimal wave guiding layer thickness, Comput. Mech. (2024).
[13] J. Friedrich, W. von Ammon, G. Müller, Czochralski growth of silicon crystals, in: Handbook of Crystal Growth, Elsevier, 2015, pp. 45–104.
[14] N. Sarukura, T. Nawata, H. Ishibashi, M. Ishii, T. Fukuda, Czochralski growth of oxides and fluorides, in: Handbook of Crystal Growth, Elsevier, 2015, pp. 131–168.
[15] M. Kirpo, Global simulation of the Czochralski silicon crystal growth in ANSYS FLUENT, J. Cryst. Growth 371 (2013) 60–69.
[16] A. Sabanskis, K. Bergfelds, A. Muiznieks, T. Schröck, A. Krauze, Crystal shape 2D modeling for transient CZ silicon crystal growth, J. Cryst. Growth 377 (2013) 9–16.
[17] X. Liu, H. Harada, Y. Miyamura, X.-f. Han, S. Nakano, S.-i. Nishizawa, K. Kakimoto, Transient global modeling for the pulling process of Czochralski silicon crystal growth. I. Principles, formulation, and implementation of the model, J. Cryst. Growth 532 (2020) 125405.
[18] J. Friedrich, T. Jung, M. Trempa, C. Reimann, A. Denisov, A. Muehe, Considerations on the limitations of the growth rate during pulling of silicon crystals by the Czochralski technique for PV applications, J. Cryst. Growth 524 (2019) 125168.
[19] A. Kondratyev, S. Demina, A. Smirnov, V. Kalaev, G. Ratnieks, L. Kadinski, A. Sattler, 3D unsteady and steady modeling of heat and mass transfer during Cz Si crystal growth with a horizontal magnetic field, Int. J. Heat Mass Transfer 178 (2021) 121604.
[20] Y. Mukaiyama, V.V. Artemyev, K. Sueoka, Numerical analysis of constitutional supercooling in heavily doped silicon crystals grown using the Czochralski method, J. Cryst. Growth 597 (2022) 126844.
[21] W. Miller, N. Abrosimov, J. Fischer, A. Gybin, U. Juda, S. Kayser, J. Janicskó-Csáthy, Quasi-transient calculation of Czochralski growth of Ge crystals using the software Elmer, Crystals 10 (1) (2019) 18.
[22] M. Saadatirad, M.H. Tavakoli, H. Khodamoradi, S.R. Masharian, Effect of the pulling, crystal and crucible rotation rate on the thermal stress and the melt–crystal interface in the Czochralski growth of germanium crystals, CrystEngComm 23 (39) (2021) 6967–6976.
[23] O. Klein, C. Lechner, P.-É. Druet, P. Philip, J. Sprekels, C. Frank-Rotsch, F.-M. Kießling, W. Miller, U. Rehse, P. Rudolph, Numerical simulation of Czochralski crystal growth under the influence of a traveling magnetic field generated by an internal Heater-Magnet Module (HMM), The Proceedings of the 15th International Conference on Crystal Growth (ICCG-15) in Conjunction with the International Conference on Vapor Growth and Epitaxy and the US Biennial Workshop on Organometallic Vapor Phase Epitaxy, J. Cryst. Growth 310 (7) (2008) 1523–1532.
[24] P. Nestler, N. Schlömer, O. Klein, J. Sprekels, F. Tröltzsch, Optimal control of semiconductor melts by traveling magnetic fields, Vietnam J. Math. 47 (4) (2019) 793–812.
[25] T.P. Nguyen, Y.-T. Hsieh, J.-C. Chen, C. Hu, H.B. Nguyen, Effect of crucible and crystal rotations on the convexity and the thermal stress in large size sapphire crystals during Czochralski growth, J. Cryst. Growth 468 (2017) 514–525.
[26] W. Miller, K. Böttcher, Z. Galazka, J. Schreuer, Numerical modelling of the Czochralski growth of β-Ga_2O_3, Crystals 7 (1) (2017) 26.
[27] C. Stelian, A. Nehari, I. Lasloudji, K. Lebbou, M. Dumortier, H. Cabane, T. Duffar, Modeling the effect of crystal and crucible rotation on the interface shape in Czochralski growth of piezoelectric langatate crystals, J. Cryst. Growth 475 (2017) 368–377.
[28] K. Böttcher, W. Miller, S. Ganschow, Numerical modeling of heat transfer and thermal stress at the Czochralski growth of neodymium scandate single crystals, Cryst. Res. Technol. 56 (1) (2021) 2000106.
[29] F. Haddad, Y.Z. Bouzouaoui, F. Mokhtari, M. Velázquez, S. Zermout, I. Lasloudji, Computational analysis of radiative heat transfer in Czochralski furnace and 3D anisotropic thermal stress in Li2MoO4 bulk crystal (crystal research and technology 10/2022), Cryst. Res. Technol. 57 (10) (2022) 2270019.
[30] A. Enders-Seidlitz, J. Pal, K. Dadzis, Development and validation of a thermal simulation for the Czochralski crystal growth process using model experiments, J. Cryst. Growth 593 (2022) 126750.
[31] V. Kalaev, D. Borisov, A. Smirnov, A modified hypothesis of Reynolds stress tensor modeling for mixed turbulent convection in crystal growth, J. Cryst. Growth 580 (2022) 126464.
[32] M.W. Scroggs, J.S. Dokken, C.N. Richardson, G.N. Wells, Construction of arbitrary order finite element degree-of-freedom maps on polygonal and polyhedral cell meshes, ACM Trans. Math. Software 48 (2) (2022) 18:1–18:23.
[33] M.W. Scroggs, I.A. Baratta, C.N. Richardson, G.N. Wells, Basix: A runtime finite element basis evaluation library, J. Open Source Softw. 7 (73) (2022) 3982.
[34] Next generation multiphysical models for crystal growth processes, https://cordis.europa.eu/project/id/851768.
[35] A. Enders-Seidlitz, J. Pal, K. Dadzis, Model experiments for Czochralski crystal growth processes using inductive and resistive heating, IOP Conf. Series: Mater. Sci. Eng. 1223 (1) (2022) 012003.
[36] VDI-Gesellschaft Verfahrenstechnik und Chemieingenieurwesen (GVC), VDI-Wärmeatlas, Springer, Berlin Heidelberg, 2006.
[37] H.D. Baehr, K. Stephan, Wärme- Und Stoffübertragung, Seventh ed., Springer-Verlag, Berlin Heidelberg New York, 2010.
[38] T. Iida, R.I.L. Guthrie, The Physical Properties of Liquid Metals, Clarendon Press, Oxford, 1993.
[39] M.V. Peralta-Martinez, W.A. Wakeham, Thermal conductivity of liquid tin and indium, Int. J. Thermophys. (2001).
[40] I.V. Savchenko, S.V. Stankus, A.S. Agadjanov, Measurement of liquid tin heat transfer coefficients within the temperature range of 506–1170 K, High Temp. 49 (4) (2011) 506–511.
[41] X. Wang, Y. Fautrelle, An investigation of the influence of natural convection on tin solidification using a quasi two-dimensional experimental benchmark, Int. J. Heat Mass Transfer 52 (23–24) (2009) 5624–5633.
[42] B.E. Abali, Computational Reality, in: Advanced Structured Materials, vol. 55, Springer, Nature, Singapore, 2017.
[43] K. Hutter, The foundations of thermodynamics, its basic postulates and implications. A review of modern thermodynamics, Acta Mech. 27 (1) (1977) 1–54.
[44] B.E. Abali, A. Queiruga, Theory and computation of electromagnetic fields and thermomechanical structure interaction for systems undergoing large deformations, J. Comput. Phys. 394 (2019) 200–231.
[45] I. Müller, W.H. Müller, Electrodynamics and rational thermodynamics, ZAMM- J. Appl. Math. Mechanics/ Z. Angew. Math. Und Mech. 103 (4) (2023) e202300209.
[46] W.F. Hughes, F.J. Young, The Electromagnetodynamics of Fluids, R.E. Krieger Pub. Co, Malabar, Florida, 1989.
[47] K. Dadzis, Modeling of Directional Solidification of Multicrystalline Silicon in a Traveling Magnetic Field (Ph.D. thesis), Technische Universität Bergakademie Freiberg, 2012.
[48] E.J. Davies, Conduction and Induction Heating, IEE Power Engineering Series 11, 1990.
[49] S. Lupi, Fundamentals of Electroheat, Springer International Publishing, Cham, 2017.
[50] C. Truesdell, R.A. Toupin, in: S. Flügge (Ed.), Encyclopedia of Physics, Volume III/1, Principles of Classical Mechanics and Field Theory, Springer- Verlag, Berlin/Göttingen/Heidelberg, 1960, pp. 226–790.
[51] B.E. Abali, F.A. Reich, Thermodynamically consistent derivation and computation of electro-thermo-mechanical systems for solid bodies, Comput. Methods Appl. Mech. Engrg. 319 (2017) 567–595.
[52] T.I. Zohdi, Electromagnetic Properties of Multiphase Dielectrics: A Primer on Modeling, Theory and Computation, vol. 64, Springer Science & Business Media, 2012.
[53] J. Stefan, Über Die Theorie Der Eisbildung, vol. 1, 1890, pp. 1–5.
[54] L.D. Landau, E.M. Lifshitz, Fluid Mechanics, second ed., Pergamon Press, Oxford, England New York, 1987.
[55] D.T.J. Hurle, Analytical representation of the shape of the meniscus in Czochralski growth, J. Cryst. Growth 63 (1) (1983) 13–17.

[56] T.I. Zohdi, Finite Element Primer for Beginners, Springer, 2018.
[57] N.S. Ottosen, H. Petersson, Introduction to the Finite Element Method, Prentice Hall, 1992.
[58] FEniC.S. Project, dolfinx v0.5.2, 2022, https://github.com/FEniCS/dolfinx/releases/tag/v0.5.2. (Accessed: 29 November 2022).
[59] A. Wintzer, M. Schröder, B.E. Abali, K. Dadzis, crystal-x, 2024, https://github.com/nemocrys/crystal-x. (Accessed: 1 April 2024).
[60] P. Virtanen, R. Gommers, T.E. Oliphant, M. Haberland, T. Reddy, D. Cournapeau, E. Burovski, P. Peterson, W. Weckesser, J. Bright, S.J. van der Walt, M. Brett, J. Wilson, K.J. Millman, N. Mayorov, A.R.J. Nelson, E. Jones, R. Kern, E. Larson, C.J. Carey, İ. Polat, Y. Feng, E.W. Moore, J. VanderPlas, D. Laxalde, J. Perktold, R. Cimrman, I. Henriksen, E.A. Quintero, C.R. Harris, A.M. Archibald, A.H. Ribeiro, F. Pedregosa, P. van Mulbregt, SciPy 1.0: Fundamental algorithms for scientific computing in Python, Nature Methods 17 (3) (2020) 261–272.
[61] A. Meurer, C.P. Smith, M. Paprocki, O. Čertík, S.B. Kirpichev, M. Rocklin, A. Kumar, S. Ivanov, J.K. Moore, S. Singh, T. Rathnayake, S. Vig, B.E. Granger, R.P. Muller, F. Bonazzi, H. Gupta, S. Vats, F. Johansson, F. Pedregosa, M.J. Curry, A.R. Terrel, Š. Roučka, A. Saboo, I. Fernando, S. Kulal, R. Cimrman, A. Scopatz, SymPy: Symbolic computing in Python, PeerJ Comput. Sci. 3 (2017) e103.
[62] C. Geuzaine, J.-F. Remacle, Gmsh: A 3-D finite element mesh generator with built-in pre- and post-processing facilities, Internat. J. Numer. Methods Engrg. 79 (11) (2009) 1309–1331.
[63] A. Meurer, C.P. Smith, M. Paprocki, O. Čertík, S.B. Kirpichev, M. Rocklin, A. Kumar, S. Ivanov, J.K. Moore, S. Singh, T. Rathnayake, S. Vig, B.E. Granger, R.P. Muller, F. Bonazzi, H. Gupta, S. Vats, F. Johansson, F. Pedregosa, M.J. Curry, A.R. Terrel, Š. Roučka, A. Saboo, I. Fernando, S. Kulal, R. Cimrman, A. Scopatz, SymPy: symbolic computing in Python, PeerJ Comput. Sci. 3 (2017) e103.